Optics Letters

Heterogeneously integrated III–V-on-lithium niobate broadband light sources and photodetectors

XIAN ZHANG,[1] XIAOYUE LIU,[1] RUI MA,[1] ZICHAO CHEN,[1] ZHUOHUI YANG,[1] YA HAN,[1] BING WANG,[1] SIYUAN YU,[1] RUIJUN WANG,[1,2] AND XINLUN CAI[1,3]

[1]State Key Laboratory of Optoelectronic Materials and Technologies, School of Electronics and Information Technology, Sun Yat-sen University, Guangzhou 510275, China
[2]e-mail: wangrj26@mail.sysu.edu.cn
[3]e-mail: caixlun5@mail.sysu.edu.cn

Received 21 June 2022; revised 2 August 2022; accepted 3 August 2022; posted 3 August 2022; published 31 August 2022

Heterogeneous integration of III–V active devices on lithium niobate-on-insulator (LNOI) photonic circuits enable fully integrated transceivers. Here we present the co-integration of InP-based light-emitting diodes (LEDs) and photodetectors on an LNOI photonics platform. Both devices are realized based on the same III–V epitaxial layers stack adhesively bonded on an LNOI waveguide circuit. The light is evanescently coupled between the LNOI and III–V waveguide via a multiple-section adiabatic taper. The waveguide-coupled LEDs have a 3-dB bandwidth of 40 nm. The photodetector features a responsivity of 0.38 A/W in the 1550-nm wavelength range and a dark current of 9 nA at −0.5 V at room temperature. © 2022 Optica Publishing Group

https://doi.org/10.1364/OL.468008

Lithium niobate (LN) has long been the primary material to develop optical modulators due to its excellent electro-optic (EO) modulation properties [1]. Traditional LN-based photonic devices are realized based on low-index-contrast ($\Delta n \approx 0.02$) titanium in-diffusion or proton exchange waveguides [2], which results in a relatively large device size. In recent years, LN-on-insulator (LNOI) wafers have become commercially available [3]. The high refractive index contrast ($\Delta n \approx 0.7$) between the LN and cladding layer leads to a strong optical confinement in the LNOI waveguide [4]. Therefore, the LNOI photonic integrated circuit emerges as a promising photonics integration platform for optical communication, sensing, and metrology applications [5,6]. Various high-performance LNOI nanophotonic components have been realized by developing advanced nanofabrication techniques [7–15]. For example, Luke *et al.* have demonstrated an LNOI waveguide with 0.27 dB/cm optical propagation loss on the wafer scale [16]. Xu *et al.* realized dual-polarization coherent LNOI modulators with sub-1-V driving voltage and 110-GHz bandwidth [17].

To realize a fully integrated optical system on a chip, light sources and photodetectors should be integrated on the LNOI photonics platform. However, the LN material cannot efficiently generate and detect light in the telecommunication wavelength range. Very recently, many efforts have been devoted to realize light sources and photodetectors integrated on the LNOI photonic integrated circuits (PICs) [18–29]. One way of doing that is to improve the light generation efficiency of LN with the help of doping rare-earth ions [28]. Optical pumped rare-earth-ions-doped LNOI micro-cavity lasers have been demonstrated in the last few years [19–23]. However, most optical systems prefer electrically pumped light sources. Compared with LN, III–V group direct-bandgap semiconductors with their lattice-matched compound semiconductors are more suitable for light generation and detection [30]. Integration of III–V materials on LNOI PICs can exploit the best characteristics from each material set. Several different approaches toward this goal have been developed, such as transfer printing, hybrid integration, flip-chip bonding, and heterogeneous integration [24–27]. Op de Beeck *et al.* demonstrated transfer-printing of III–V-on-LN amplifiers and lasers on LNOI PICs [24]. In those devices, the light is evanescently coupled from the III–V active region to the LNOI waveguide via a microtransfer-printed silicon interlayer. The evanescent coupling among the III–V, silicon, and LNOI waveguide requires a high lateral alignment accuracy, but the alignment accuracy of current transfer printing technology is limited [31,32], which results in a higher coupling loss and less gain than the bonded devices. Shams-Ansari *et al.* demonstrated the integration of pre-fabricated III–V semiconductor lasers with LNOI by flip-chip bonding [26]. A high optical power of 60 mW coupled into the LNOI waveguides is achieved, but the mode mismatching between the III–V and LN waveguide results in an optical coupling loss of approximately 5 dB. In addition, the flip-chip bonding of individual lasers is time consuming and not suitable for high volume manufacturing. Very recently, Guo *et al.* reported the heterogeneous integration of modified uni-traveling carrier photodiodes on LNOI waveguides using SU8 as the adhesive bonding agent [27]. A responsivity of 0.6 A/W and a bandwidth of 80 GHz is achieved at 1550-nm wavelength. However, the III–V material is only applicable for photodetection, and the integration of light sources requires another extra III–V epitaxial layer stack and fabrication process.

In this Letter, we present the heterogeneous integration of III–V active devices on LNOI PICs by adhesive bonding. The light source and photodetector are realized based on the same III–V material, thus enabling a fully integrated optical system by

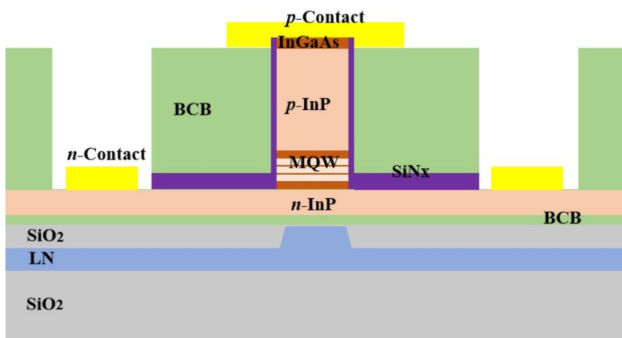

Fig. 1. Schematic of the cross section of the III–V-on-LNOI photonic device.

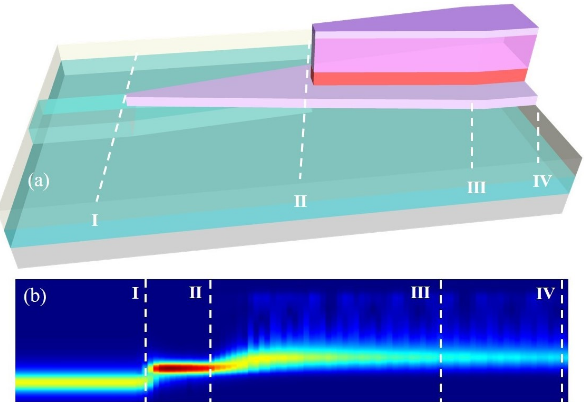

Fig. 2. (a) Schematic of the coupling structure. (b) Intensity distribution in the designed taper structure.

bonding only one III–V epitaxial layer stack on the LNOI PIC. A multiple-section spot size converter is designed to achieve efficient optical coupling between the III–V and LNOI waveguide. The heterogeneously integrated photodetector has a responsivity of 0.38 A/W at the wavelength of 1540 nm and a dark current of 9 nA at −0.5 V at room temperature. This integration approach enables wafer scale fabrication of III–V-on-LNOI optical systems.

Figure 1 shows the schematic of the cross section of the heterogeneously integrated III–V-on-LNOI photonic device. The III–V epitaxial layer stack is adhesively bonded to a LNOI waveguide circuit using a 70-nm-thick benzocyclobutene (DVS-BCB) polymer layer as the bonding agent. The III–V stack consists of 300-nm-thick n-InP layer ($\sim 1 \times 10^{18}$ cm^{-3}), an AlGaInAs active region surrounded by two 120-nm separate confinement heterostructure (SCH) layers, a 1.6-μm-thick p-InP cladding layer, and 200-nm p-InGaAs contact layer ($\sim 1.5 \times 10^{19}$ cm^{-3}). Under the III–V stack, the LN layer is 360-nm-thick rib waveguide etched 180-nm deep. A combination of SiN_x and DVS-BCB layers are employed to passivate the III–V waveguide.

For the III–V-on-LNOI photonic devices, phase matching is necessary for an efficient optical coupling between the III–V active waveguide and LNOI passive waveguide. As the refractive index of the III–V material is much higher the LN material at the wavelength of 1550 nm, a multiple-section taper is designed to achieve index matching. The coupling structure can be divided into four parts, as schematically shown in Fig. 2(a). In the right of the structure, the optical mode is confined in the III–V waveguide, which works as a gain section for light sources and an absorption section for photodetectors. The light is evanescently coupled from the III–V waveguide to the underneath of the LNOI waveguide via two tapered sections. To achieve efficient coupling and reduce the reflection, an ultra-narrow III–V taper tip is required. Considering the resolution of the electron beam lithography and dry etching process, the tip width is designed to be 150 nm. In the first III–V taper section, the light is coupled from the active region to the n-InP layer. According to simulation, the coupling efficiency is approximately 90% when the width of the p-InP cladding layer and active region were tapered from 2.5 μm to 0.15 μm. In the second taper section, the light is coupled from the n-InP layer to the LNOI waveguide. The simulated coupling efficiency reaches 90% when the n-InP taper tip is 0.15-μm wide. So, the total coupling efficiency of the taper is approximately 81%. The coupling efficiency can be further improved to 95% by reducing the BCB thickness to 30 nm. Figure 2(b) shows the fundamental mode intensity distribution in a longitudinal cross section of the taper structure. The use of a direct transition between the lithium niobate waveguide and the III–V waveguide instead of using an intermediate layer can improve the bonding yield and reduce the difficulties of device fabrication. The saturation output powers of the semiconductor optical amplifier can be improved by adjusting the III–V layer stack design (e.g., increasing the III–V waveguide layer thickness).

The passive LN PICs are processed on a X-cut LNOI wafers with a 360-nm-thick LN device layer and 2-μm-thick buried oxide layer. The LN layer is etched 180-nm deep in the waveguide fabrication. Before bonding, a SiO_2 layer is deposited by plasma enhanced chemical vapor deposition, followed by chemical mechanical polishing (CMP) down to the LN device layer. Afterward, the InP-based epitaxial stack is adhesively bonded to the LN PIC. Then the InP substrate is removed using a 3:1 HCl:H_2O solution. The InP mesa is patterned by electron beam lithography (EBL) and etched by inductively coupled plasma (ICP) until the n-InP contact layer. Then a 200-nm SiN_x layer is deposited on the sample as a hard mask for the dry etching of the n-InP layer. After the dry etching, Ni/Ge/Au is deposited as the n-contact, which is 10 μm away from the edge of the III–V mesa. Subsequently, DVS-BCB is spin-coated on the sample and cured at 250°C for 2 hours to passivate the device. Then the DVS-BCB layer is dry etched to open the window for the p-contact and n-contact deposition. Finally, Ti/Pt/Au is deposited as p-contact and annealed at 380°C for 10 minutes. Figure 3(a) shows the top view optical microscopy image of the fabricated heterogeneously integrated III–V-on-LN device. A scanning electron microscopy (SEM) image of cross section of the part III of the fabricated device is shown in Fig. 3(b). The propagation loss of the LNOI waveguide is approximately 0.2 dB/cm. Since there are ~70-nm-thick BCB and silicon dioxide layers above the LNOI waveguide layer, the dry etching of the III–V taper can be controlled to avoid the etching of the LN layer.

The heterogeneously integrated III–V-on-LN photonic devices are characterized at room temperature. The waveguide-coupled light-emitting diodes (LEDs) consist of a 3-μm-wide and 500-μm-long III–V waveguide. The spontaneous emission is coupled from the III–V waveguide to the LN waveguide via a multiple-section taper with a tip width of 150 nm. The light is coupled out through an on-chip LN grating coupler and collected by a single-mode fiber. Figure 4 shows the electroluminescence

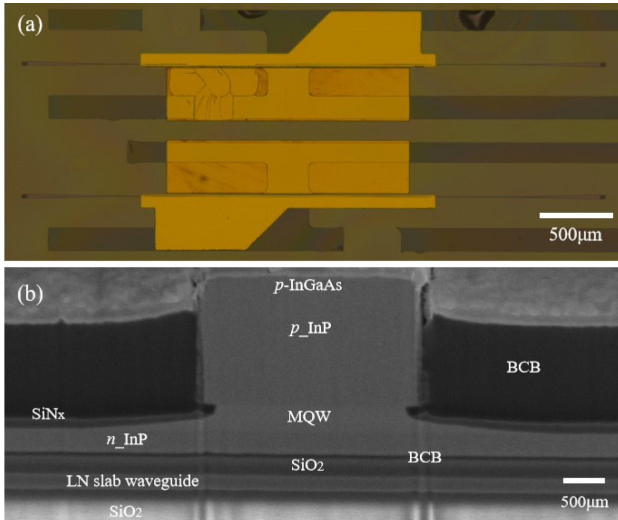

Fig. 3. (a) Optical microscopy image of the heterogeneously integrated III–V-on-LN device. (b) SEM image of the cross section of the fabricated devices.

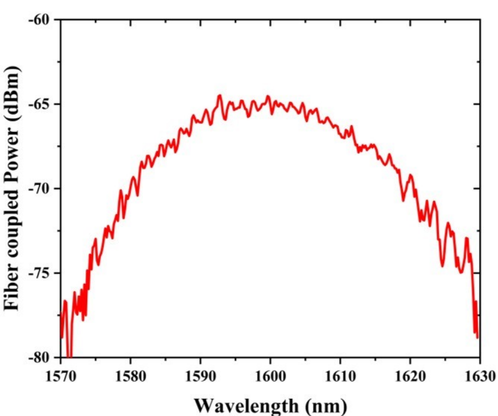

Fig. 4. Electroluminescence spectrum of the heterogeneously integrated LED.

spectrum from a III–V-on-LN LED. The spectrum has a 3-dB bandwidth of 40 nm centered at 1600 nm. The spectrum measured by the fiber is the superposition of the spontaneous emission spectrum and the grating spectrum. To obtain the spontaneous emission spectrum of the LED, the grating spectrum should be to be subtracted. The grating efficiency at 1600 nm is approximately −12 dB.

Figure 5(a) shows a typical current–voltage (I–V) curve of the heterogeneously integrated III–V-on-LN photodetector without light input. A high-resolution source meter (Keithley 2400) is used to measure the I–V characteristics of the photodetector. The measured dark current is 9 nA and 65 nA under reverse bias voltage of 0.5 V and 2 V, respectively. In the measurement of the responsivity, the light is coupled into the LN waveguide through a single-mode fiber with the help of an on-chip grating coupler. A polarization controller is used to maintain the input light in TE polarization. The coupler has peak coupling efficiency of approximatelyt −6 dB at 1550 nm with a 3-dB bandwidth of ~50 nm. Figure 5(b) shows the I–V curve of the device under different waveguide-coupled input powers at the wavelength of

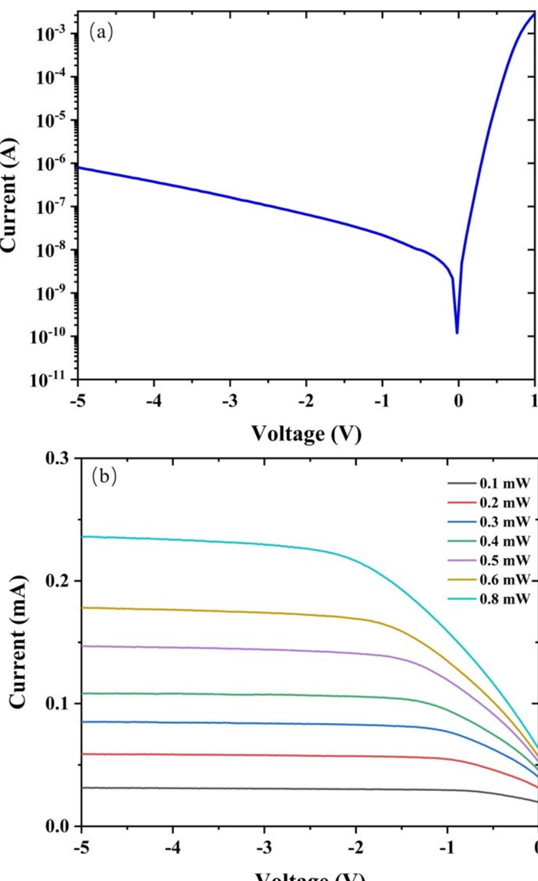

Fig. 5. (a) I–V curve of the III–V-on-LN photodetector without light input. (b) I–V curve of the photodetector under illumination at the wavelength of 1550 nm.

1550 nm. The actual power coupled to the LN waveguide is determined by measuring the coupling efficiency of the reference grating coupler on the same sample. The input light power varies from 0.1 mW to 0.8 mW with a step of 0.1 mW. A higher voltage is required to extract the photon-generated carrier when the input power increases. The waveguide-referred responsivity is approximately 0.3 A/W at −2 V, which corresponds to a quantum efficiency of 24%.

Figure 6 shows the waveguide-coupled spectral response between 1520 and 1590 nm of the photodetector biased at −2 V. The responsivity is higher than 0.15 A/W over the wavelength range of 1520–1580 nm. The measured peak waveguide-coupled responsivity is 0.38 A/W at 1540 nm. The absorption coefficient of quantum wells is larger in the shorter wavelength region. So, the responsivity peak locates in the short wavelength side close to the peak of the spontaneous emission spectrum. As the photon energy is less than the bandgap energy of the active region, the responsivity dramatically decreases at longer wavelength. The coupling efficiency and photodetector responsivity can be further improved by reducing the thickness of the BCB (to be less than 30 nm) and silicon oxide layers between the III–V and lithium niobite waveguide.

In this Letter, we demonstrate the heterogeneous integration of III–V broadband light sources and photodetectors on LNOI waveguide circuits. A multiple-section taper structure is designed to achieve an efficient coupling between the active

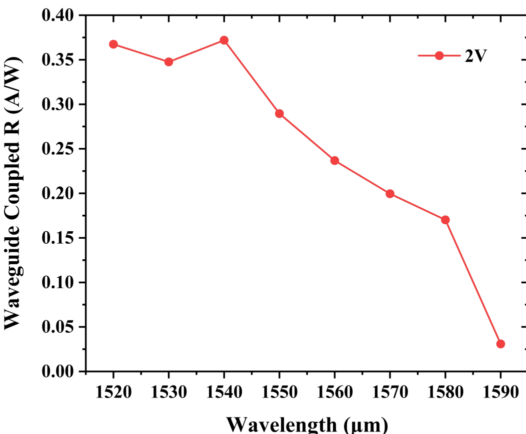

Fig. 6. Waveguide coupled responsivity as a function of wavelength at the reverse bias voltage of 2 V.

III–V waveguide and passive LN waveguide. The emission spectrum of the integrated LED exhibits a 3-dB bandwidth of 40 nm centered at 1600 nm. The integrated photodetectors have a low dark current of 9 nA at −0.5 V and peak responsivity of 0.38 A/W at 1540 nm. The light sources and photodetectors are realized based on the same III–V material, thereby enabling completely integrated optic systems by heterogeneous integration of only one III–V epitaxial layer stack on the LNOI waveguide circuit. The 150-nm-wide III–V taper tip can also be patterned by 193-nm DUV lithography, thereby enabling wafer-scale fabrication of III–V-on-LNOI photonic devices by combining the wafer bonding technique with DUV lithography.

Funding. National Key Research and Development Program of China (2019YFB2203302); Local Innovative and Research Teams Project of Guangdong Pearl River Talents Program (2017BT01X121); Key R&D Program of Guangdong Province (2018B030329001); Basic and Applied Basic Research Foundation of Guangdong Province (2022A1515012634); Fundamental Research Funds for the Central Universities, Sun Yeat-sen University (22QNTD0502).

Disclosures. The authors declare no conflicts of interest.

Data availability. Data underlying the results presented in this Letter are not publicly available at this time but may be obtained from the authors upon reasonable request.

REFERENCES

1. R. S. Weis and T. K. Gaylord, Appl. Phys. A **37**, 191 (1985).
2. E. L. Wooten, K. M. Kissa, A. Yi-Yan, E. J. Murphy, D. A. Lafaw, P. F. Hallemeier, D. Maack, D. V. Attanasio, D. J. Fritz, G. J. McBrien, and D. E. Bossi, IEEE J. Sel. Top. Quantum Electron. **6**, 69 (2000).
3. P. Rabiei and P. Gunter, Appl. Phys. Lett. **85**, 4603 (2004).
4. G. Poberaj, H. Hu, W. Sohler, and P. Günter, Laser Photonics Rev. **6**, 488 (2012).
5. J. Lin, F. Bo, Y. Cheng, and J. Xu, Photonics Res. **8**, 1910 (2020).
6. D. Zhu, L. Shao, M. Yu, R. Cheng, B. Desiatov, C. J. Xin, Y. Hu, J. Holzgrafe, S. Ghosh, A. Shams-Ansari, E. Puma, N. Sinclair, C. Reimer, M. Zhang, and M. Lončar, Adv. Opt. Photonics **13**, 242 (2021).
7. C. Wang, M. Zhang, X. Chen, M. Bertrand, A. Shams-Ansari, S. Chandrasekhar, P. Winzer, and M. Loncar, Nature **562**, 101 (2018).
8. M. Zhang, B. Buscaino, C. Wang, A. Shams-Ansari, C. Reimer, R. Zhu, J. M. Kahn, and M. Loncar, Nature **568**, 373 (2019).
9. Z. Lin, Y. Lin, H. Li, M. Xu, M. He, W. Ke, H. Tan, Y. Han, Z. Li, D. Wang, X. S. Yao, S. Fu, S. Yu, and X. Cai, Light: Sci. Appl. **11**, 1 (2022).
10. X. Han, L. Chen, Y. Jiang, A. Frigg, H. Xiao, T. G. Nguyen, A. Boes, J. Yang, G. Ren, Y. Su, A. Mitchell, and Y. Tian, Laser Photonics Rev. **16**, 2200130 (2022).
11. Z. Ma, J. Y. Chen, Z. Li, C. Tang, Y. M. Sua, H. Fan, and Y. P. Huang, Phys. Rev. Lett. **125**, 263602 (2020).
12. J.-Y. Chen, Z.-H. Ma, Y. M. Sua, Z. Li, C. Tang, and Y.-P. Huang, Optica **6**, 1244 (2019).
13. M. Zhang, C. Wang, R. Cheng, A. Shams-Ansari, and M. Lončar, Optica **4**, 1536 (2017).
14. B. Pan, H. Cao, Y. Huang, Z. Wang, K. Chen, H. Li, Z. Yu, and D. Dai, Photonics Res. **10**, 697 (2022).
15. L. Cortes-Herrera, X. He, J. Cardenas, and G. P. Agrawal, Opt. Express **29**, 44174 (2021).
16. K. Luke, P. Kharel, C. Reimer, L. He, M. Loncar, and M. Zhang, Opt. Express **28**, 24452 (2020).
17. M. Xu, Y. Zhu, F. Pittalà, J. Tang, M. He, W. C. Ng, J. Wang, Z. Ruan, X. Tang, M. Kuschnerov, L. Liu, S. Yu, B. Zheng, and X. Cai, Optica **9**, 61 (2022).
18. B. Desiatov and M. Lončar, Appl. Phys. Lett. **115**, 121108 (2019).
19. D. Yin, Y. Zhou, Z. Liu, Z. Wang, H. Zhang, Z. Fang, W. Chu, R. Wu, J. Zhang, W. Chen, M. Wang, and Y. Cheng, Opt. Lett. **46**, 2127 (2021).
20. J. Zhou, Y. Liang, Z. Liu, W. Chu, H. Zhang, D. Yin, Z. Fang, R. Wu, J. Zhang, W. Chen, Z. Wang, Y. Zhou, M. Wang, and Y. Cheng, Laser Photonics Rev. **15**, 2100030 (2021).
21. R. Zhang, C. Yang, Z. Hao, D. Jia, Q. Luo, D. Zheng, H. Liu, X. Yu, F. Gao, F. Bo, Y. Kong, G. Zhang, and J. Xu, Sci. China Phys. Mech. Astron. **64**, 294216 (2021).
22. Z. Xiao, K. Wu, M. Cai, T. Li, and J. Chen, Opt. Lett. **46**, 4128 (2021).
23. X. Liu, X. Yan, Y. Liu, H. Li, Y. Chen, and X. Chen, Opt. Lett. **46**, 5505 (2021).
24. C. Op de Beeck, F. M. Mayor, S. Cuyvers, S. Poelman, J. F. Herrmann, O. Atalar, T. P. McKenna, B. Haq, W. Jiang, J. D. Witmer, G. Roelkens, A. H. Safavi-Naeini, R. Van Laer, and B. Kuyken, Optica **8**, 1288 (2021).
25. Y. Han, X. Zhang, F. Huang, X. Liu, M. Xu, Z. Lin, M. He, S. Yu, R. Wang, and X. Cai, Opt. Lett. **46**, 5413 (2021).
26. A. Shams-Ansari, D. Renaud, R. Cheng, L. Shao, L. He, D. Zhu, M. Yu, H. R. Grant, L. Johansson, M. Zhang, and M. Lončar, Optica **9**, 408 (2022).
27. X. Guo, L. Shao, L. He, K. Luke, J. Morgan, K. Sun, J. Gao, T.-C. Tzu, Y. Shen, D. Chen, B. Guo, F. Yu, Q. Yu, M. Jafari, M. Lončar, M. Zhang, and A. Beling, Photonics Res. **10**, 1338 (2022).
28. A. J. Kenyon, Prog. Quantum Electron. **26**, 225 (2002).
29. Z. Wang, Z. Fang, Z. Liu, W. Chu, Y. Zhou, J. Zhang, R. Wu, M. Wang, T. Lu, and Y. Cheng, Opt. Lett. **46**, 380 (2021).
30. S. Mokkapati and C. Jagadish, Mater. Today **12**, 22 (2009).
31. S. Dhoore, S. Uvin, D. Van Thourhout, G. Morthier, and G. Roelkens, Opt. Express **24**, 12976 (2016).
32. B. Haq, S. Kumari, K. Van Gasse, J. Zhang, A. Gocalinska, E. Pelucchi, B. Corbett, and G. Roelkens, Laser. Photon. Rev **14**, 1900364 (2020).